# University of Groningen

## Performance of MACACO Compton telescope for ion-beam therapy monitoring

Solevi, Paola; Munoz, Enrique; Solaz, Carles; Trovato, Marco; Dendooven, Peter; Gillam, John E.; Lacasta, Carlos; Oliver, Josep F.; Rafecas, Magdalena; Torres-Espallardo, Irene

**IMPORTANT NOTE: You are advised to consult the publisher's version (publisher's PDF) if you wish to cite from it. Please check the document version below.**

*Document Version*
Publisher's PDF, also known as Version of record

[Link to publication in University of Groningen/UMCG research database](#)

**PAPER**

# Performance of MACACO Compton telescope for ion-beam therapy monitoring: first test with proton beams

View the article online for updates and enhancements.

**IPEM | IOP**

Series in Physics and Engineering in Medicine and Biology

Your publishing choice in medical physics, biomedical engineering and related subjects.

Start exploring the collection–download the first chapter of every title for free.

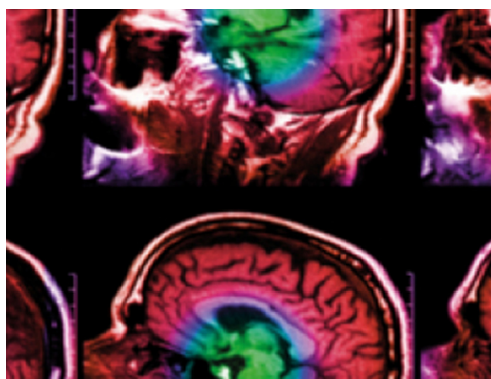# Performance of MACACO Compton telescope for ion-beam therapy monitoring: first test with proton beams

**Paola Solevi[1,4], Enrique Muñoz[1], Carles Solaz[1], Marco Trovato[1], Peter Dendooven[2,3], John E Gillam[1,5], Carlos Lacasta[1], Josep F Oliver[1], Magdalena Rafecas[1,6], Irene Torres-Espallardo[1,7] and Gabriela Llosá[1]**

[1] Instituto de Fìsica Corpuscular (IFIC-CSIC/UVEG), Valencia, Spain
[2] KVI-Center for Advanced Radiation Technology, University of Groningen, Groningen, The Netherlands
[3] Helsinki Institute of Physics, Helsinki, Finland

E-mail: paola.solevi@ovgu.de

## Abstract

In order to exploit the advantages of ion-beam therapy in a clinical setting, delivery verification techniques are necessary to detect deviations from the planned treatment. Efforts are currently oriented towards the development of devices for real-time range monitoring. Among the different detector concepts proposed, Compton cameras are employed to detect prompt gammas and represent a valid candidate for real-time range verification. We present the first on-beam test of MACACO, a Compton telescope (multi-layer Compton camera) based on lanthanum bromide crystals and silicon photo-multipliers. The Compton telescope was first characterized through measurements and Monte Carlo simulations. The detector linearity was measured employing $^{22}$Na and Am-Be sources, obtaining about 10% deviation from linearity at 3.44 MeV. A spectral image reconstruction algorithm was tested on synthetic data. Point-like sources emitting gamma rays with energy between 2 and 7 MeV were reconstructed with 3–5 mm resolution. The two-layer Compton telescope was employed to measure radiation emitted from a beam of 150 MeV protons impinging on a cylindrical PMMA target. Bragg-peak shifts were achieved via adjustment of the PMMA target location and the resulting

measurements used during image reconstruction. Reconstructed Bragg peak profiles proved sufficient to observe peak-location differences within 10 mm demonstrating the potential of the MACACO Compton Telescope as a monitoring device for ion-beam therapy.

(Some figures may appear in colour only in the online journal)

## 1. Introduction

Ion-beam therapy provides an effective tumor treatment modality combining high dose conformity with enhanced radiobiological effectiveness with respect to conventional radiation therapy (Schardt *et al* 2010). However, treatment delivery verification techniques are necessary to fully exploit the advantages of ion-beam therapy in the clinical setting. Several monitoring techniques have been envisaged and studied in the last decade, each technique oriented at detecting secondary radiation exiting the patient which is produced by the interaction of the primary projectiles with patient tissue, as described in Knopf *et al* (2013). To date, the most widely explored technique has been positron emission tomography (PET) (Enghardt *et al* 1999), that images the distribution of the vertices of annihilation gamma rays following the decay of positron-emitter nuclei induced in the patient. While PET is capable of providing a 3D verification of the treatment delivery, its integration in-beam may imply a high cost and performance can be further constrained by accelerator features. In-room PET represents then an optimum solution, providing good data quality at a reasonable integration effort (Shakirin *et al* 2011). As a consequence efforts are currently being made towards the development of real-time range monitoring techniques that also avoid distortion due to biological washout. For this reason attention has been drawn to prompt gammas which are emitted by excited nuclei within few ps after the passage of the primary ion (Min *et al* 2006) and are produced in abundance during ion therapy treatment (Pinto *et al* 2015). The emission energy of prompt gammas from proton interaction in tissue typically ranges between 2 and 7 MeV (Polf *et al* 2009, Verburg *et al* 2013). The detection, identification and vertex reconstruction of prompt gammas pose several challenges requiring dedicated detector designs. Different range verification approaches based on prompt gamma detection have been suggested. Mechanically collimated prompt gamma cameras have been studied (Smeets *et al* 2012, Pinto *et al* 2014) that yield at least one-dimensional beam profiles. In Golnik *et al* (2014) range assessment is performed through timing measurements of the prompt gamma rays based on the correlation between the ion penetration path in patient tissue and the finite ion transit time, typically between 1 and 2 ns at therapeutic energies. Different prototypes of electronically collimated gamma cameras have also been investigated (Peterson *et al* 2010, Kormoll *et al* 2011, Polf *et al* 2015). Electronically collimated gamma cameras have a larger angular acceptance to incident prompt gammas. However to be effectively translated into a sensitivity gain, increased efforts are required in electronics and software for event processing and reconstruction.

In this paper we present the first on-beam test of MACACO (medical application compact Compton camera), a Compton telescope (multi-layer Compton camera) based on lanthanum bromide ($LaBr_3$) crystals and silicon photo-multipliers (Llosá *et al* 2013a, Llosá *et al* 2016). Each layer consists of a monolithic scintillating crystal read-out by a matrix of silicon photo-multipliers (SiPMs). The current prototype consists of three layers allowing double and triple coincidences within the three modules in order to track the incoming

gamma ray. The detection of either two-interaction events with photo-absorption or more than two interactions makes the determination of the incoming gamma energy possible. However the high emission energy of the prompt gammas reduces the full-absorption probability in two-interaction events. Even in the case of photo-absorption the unknown energy of the incident gamma has to be estimated over the wide prompt gamma emission spectrum. Three-interaction events have the drawback of reduced efficiency, increased random fraction and higher complexity in event ordering. Two-interaction events are the easiest to handle yet require dedicated Compton image reconstruction approaches to infer the emission spectra of the prompt gamma. While the prototype allows both two-layer (Llosá *et al* 2013b) and three-layer (Llosá *et al* 2016) operation, the results presented here focus on the two-layer system. The prototype has been tested on-beam at the irradiation facility of the AGOR cyclotron at KVI-Center for Advanced Radiation Technology, University of Groningen, the Netherlands. A PMMA target was irradiated by 150 MeV protons at therapeutic beam current and detected radiation spectra in single acquisition mode have been measured. The PMMA phantom was also measured in coincidence acquisition mode at two different locations 10 mm apart and the reconstructed profiles are presented, providing the first proof of the capability of the system to detect range shifts. Throughout the manuscript the experimental data analysis is accompanied by results obtained from Monte Carlo simulations of the different scenarios. Simulations were used to support the understanding of measured data, determine background rejection criteria and assess the efficiency and spatial resolution of the detector in each set-up employed.

## 2. Materials and methods

### 2.1. Compton telescope description

The prototype is composed of three detector layers, each one consisting of a monolithic $LaBr_3$ scintillating crystal coupled to a matrix of SiPMs (Llosá *et al* 2016). The third layer, also described in this section, was present but disconnected in the work presented here due to a failure of one of the components in the readout electronics board. The first layer is made of a $27.2 \times 26.8 \times 5$ mm$^3$ $LaBr_3$ crystal coupled to four SiPM arrays. Each SiPM array consists of $4 \times 4$ multi-pixel photon-counters (MPPCs) from Hamamatsu Photonics (S11830-3344MF). The second and third layers consist of $32 \times 36 \times 5$ mm$^3$ and $32 \times 36 \times 10$ mm$^3$ monolithic $LaBr_3$ crystals, respectively. Each crystal is coupled to four MPPC arrays from Hamamatsu Photonics (S11064-050P(X1)). Each MPPC of the three layers is $3 \times 3$ mm$^2$ with 3600 microcells. The second and third layer MPPCs have a pitch of $4.05 \times 4.5$ mm$^2$ while the first layer has $3.2 \times 3.2$ mm$^2$ pitch. The choice of monolithic crystals coupled to a matrix of $8 \times 8$ MPPCs with such a microcell size has been selected with the aim of having good dynamic range and linearity up to several MeV energy.

Each detector is attached to a custom-made printed circuit board (PCB) that both provides mechanical support and hosts the ASIC read-out chip. The hybrid PCB provides individual bias voltage to each array on the first layer, while a single input bias is applied to the second and third layer, respectively. The front-end and the back-end electronics are decoupled resulting in a very flexible modular design (see figure 1). The front-end read-out chip is based on the 64-channel charge sensitive amplifier VATA64HDR16 ASIC (Meier *et al* 2010). The first stage in the ASIC is a preamplifier with two possible input gains. An 8-bit DAC allows the user to fine-trim the potential at the input of the preamplifier from 0 to 1 V. This allows the operating voltage of each pixel to be adjusted independently. After the preamplifier the signal goes to the slow shaper, a semi-Gaussian filter that provides
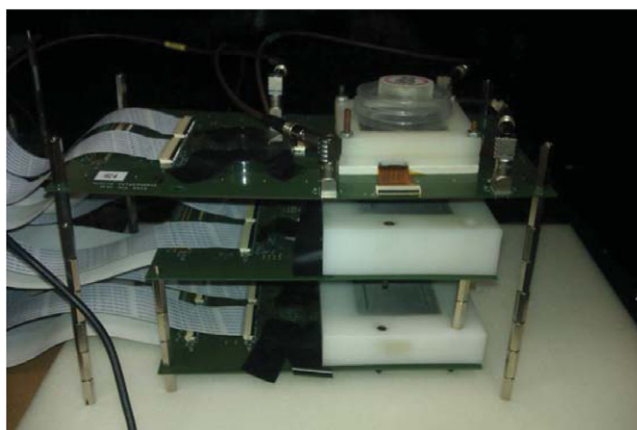
**Figure 1.** Picture of the three-layer Compton telescope in the laboratory set-up.

energy information either in a voltage or a current signal, depending on the user's choice. A sample and hold unit allows the energy in each channel to be captured when the appropriate control is enabled. The sampled signal for each channel is sent to the DAQ (data acquisition) board (Stankova *et al* 2012). The FPGA on the DAQ board is able to program biases for the ASIC, manage the readout process, configure the ASIC and switch between different trigger modes (single or coincidence acquisition mode). When an event takes place, the front-end ASIC generates a trigger signal which is transmitted to the FPGA. At this moment the readout sequence starts. The DAQ board is managed by an FPGA (XC3S4000 from Xilinx) that receives instructions from a software application used to control the board via a 10/100/1000 Mbps Ethernet connection, using the UDP protocol. The energy value for each of the 64 channels is sampled by the ASIC and the values are recovered in series. After the readout process, the analog data coming from the hybrid reaches the DAQ board, where it is amplified and digitized by a 12-bit ADC. Each packet is marked with an event counter and a time-stamp provided by an embedded TDC in the FPGA. The temperature on the surface of the hybrid is also acquired from a DS18B20 digital sensor with $\pm0.5$ °C precision. Then the data is formatted into data packets and sent to the computer via ethernet for further processing.

The detectors' performance has been characterized. The best energy resolution achieved was 6.4% and 7.4% (FWHM at 511 keV) for the first and second layer, respectively (Llosá *et al* 2016). The response of each MPPC element in the arrays has been monitored and equalized to within 1.5% by the preamplifier DAC. The timing resolution measured with the two detectors in coincidence was 25 ns (FWHM) due mainly to time-walk (Barrio *et al* 2015). The gamma ray interaction position was determined using a method based on an analytical model that was solved iteratively using a non-linear least squares data fitting (Li *et al* 2010, Cabello *et al* 2015). The model was based on the solid angle subtended by the estimated position of interaction by every MPPC pixel, considering reflections at each side of the crystal. A spatial resolution of 1.25 mm (FWHM) was measured at 511 keV energy (Llosá *et al* 2013b). This algorithm does not allow reconstruction of multiple-interaction events occurring within the same crystal. Cluster-finding techniques shall be applied in order to identify and reject multiple interactions. In this work multiple interactions within the same scintillating crystal were not identified and were reconstructed as single interaction events. Additionally no Compton kinematic ordering was applied, thus assigning the first interaction to the detector closest to the gamma emission vertex.
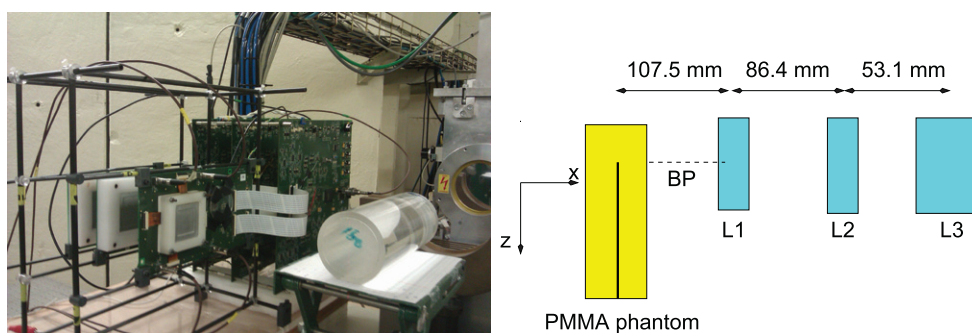
**Figure 2.** Left: picture of the experimental set-up at the KVI-CART facility. The first detector is positioned 10.75 cm from the beam axis. The system is centered at the calculated Bragg peak location of the proton beam within the PMMA target. Right: schematic drawing of the set-up (not to scale). The beam direction is $-\bar{z}$.

### 2.2. Detector characterization

The MPPCs show a strong temperature dependence of the breakdown voltage that translates into gain variation. The possibility to monitor and record the temperature, event-by-event, during data acquisition allows for offline gain correction avoiding the use of a cooling system or bias voltage tuning. In order to apply temperature corrections to the data taken in beam, the temperature dependence of the detector has been characterized. The bias voltage was set at a reference temperature $T_0$ and spectra of a $^{22}$Na source have been acquired in a climate chamber at different temperature variations $\Delta T = T - T_0$. From the measured position of the 511 keV and 1275 keV photopeaks at different temperatures, the gain variation $\alpha = \Delta G / \Delta T$ was computed (where $G$ is the gain of the detector). The temperature coefficient $\alpha$ was fitted by the function:

$$\mathrm{ADC}^{\mathrm{corr}}(T) = \mathrm{ADC}(T)(1 + \alpha \Delta T)^{-1}. \tag{1}$$

The detector energy calibration was also carried out. In the present work a first attempt to calibrate the detector and test its linearity at higher energies is presented. Energy calibration was conducted by measuring a $^{22}$Na source and the gamma rays emitted by an Am-Be source. The $^{241}$Am emits an $\alpha$-particle that interacts with the Beryllium through $^9Be(\alpha, n)^{12}C$, producing a 4.44 MeV gamma ray plus a neutron. The $^{241}$Am source activity was 37 MBq.

### 2.3. On-beam experiments at KVI-CART

The Compton telescope was tested on-beam at the irradiation facility of the AGOR cyclotron at KVI-Center for Advanced Radiation Technology, University of Groningen, the Netherlands. The AGOR cyclotron can deliver proton beams with energy between 40 MeV and 190 MeV. All experiments were performed with proton beams with fixed energy of 150 MeV and intensity of about $10^8$ protons s$^{-1}$. The proton beam current is monitored by an air ionization chamber. The lateral beam spread was 5.3 mm FWHM. The Compton telescope was installed as in figure 2. As described in section 2.1, the three-layer set-up was installed. However results reported refer to the two-layer system in which the third layer was electronically disconnected. The three detectors are supported by a structure made of carbon fiber tubes in order to minimize the amount of material surrounding the detectors (see figure 2). The structure, however, does not allow a very precise positioning of the detectors. A PMMA ($C_5H_8O_2$, $\rho = 1.19$ g cm$^{-3}$) cylindrical target 163 mm long and 60 mm diameter was irradiated by 150 MeV protons with

**Table 1.** Summary of the measurements performed at the KVI-CART facility and presented in the manuscript.

| Phantom | $z_{BP}$ (mm) | Trigger mode | Proton current (protons s$^{-1}$) |
|---------|---------------|--------------|-----------------------------------|
| PMMA | 0 | Single | $9 \cdot 10^7$ |
| PMMA | $\pm 5$ | Coincidence | $9 \cdot 10^7$ |

*Note*: A PMMA target was irradiated by 150 MeV protons. Data were acquired in both single and coincidence mode, the latter at two different target locations.

Bragg-peak located at 136 mm depth. Data were acquired in different modalities, either in coincidence or single mode. A summary of the measurements performed, and presented throughout this manuscript, can be found in table 1. Due to the system time resolution (see section 2.1), in coincidence mode a relatively large coincidence window of 40 ns was applied likely inducing a large fraction of random events in the measured spectra. Data were acquired with the PMMA target placed at two different locations, $\pm 5$ mm, in order to mimic the shift of the Bragg Peak without altering the irradiation parameters (proton energy, intensity, and beam spread).

### 2.4. GATE simulations

The Compton telescope was also modeled by means of GATE version 7.1 (Jan *et al* 2004). GATE is a Monte Carlo tool based on Geant4 classes (Agostinelli *et al* 2003), developed in order to simulate medical imaging devices. GATE offers the user several features for easy modeling of complex sources and electronics read-out. In simulations, each crystal was composed of LaBr$_3$ with density 5.08 g cm$^{-3}$. The three layers are located as in the experimental set-up described in figure 2. The standard electromagnetic and the hadronic QGSP_BIC_HP physics lists were selected for the simulation of the PMMA target irradiation. The SiPM matrix was not modeled in the simulation, so the position of the gamma ray interaction was computed from the centre of gravity of the different energy depositions (hits) occurring within each sensitive volume. An energy resolution of 8% (FWHM) at 511 keV was applied. A time blurring of 8 ns ($\sigma$) was also applied. Detected interactions in the first two detectors were externally sorted into coincidences by applying a 40 ns coincidence window. If single mode is selected, instead of coincidence, then all events yielding a signal in at least one detection volume were considered. The phase-space of particles exiting the phantom and entering the individual scintillating crystal was also stored, allowing further selection and inspection of the detected spectra.

*2.4.1. Am-Be source.* The Am-Be source was simulated in order to understand the measured spectra and assign the proper energy to visible peaks. It was simulated as a point-like neutron and gamma source with the same emission rates for both particles. The neutron emission spectrum was extracted from (Marsh *et al* 1995) and is shown in figure 3.

*2.4.2. Mono-energetic gamma rays.* In order to study the detection efficiency of double interaction events and their reconstructed spatial resolution at different energies, an initial set of simulations was computed with mono-energetic point-like sources. The energies considered are those relevant to nuclei de-excitation and the associated inelastic proton interactions and range between 2.74 and 7.12 MeV. A summary of the gamma ray energies and production mechanisms can be found in table 2 (Polf *et al* 2009, Verburg *et al* 2013). The gamma
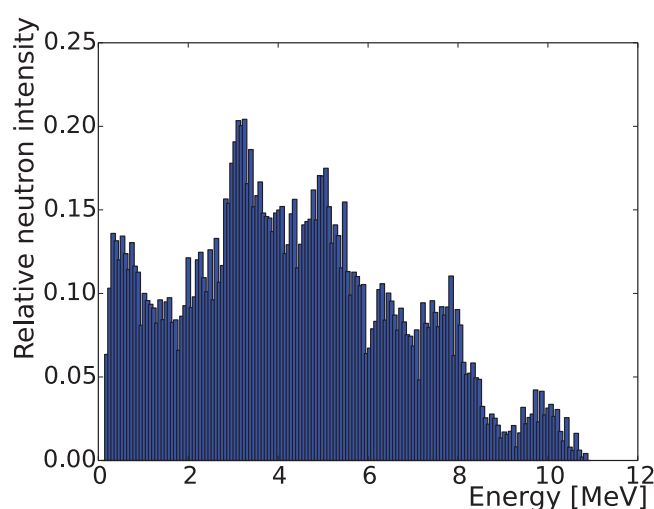
**Figure 3.** Simulated emission spectrum of the neutrons produced by an Am-Be source. The emission spectrum is extracted from (Marsh *et al* 1995).

**Table 2.** List of some important reactions yielding prompt gamma rays to be detected by the Compton telescope, for carbon and oxygen target nuclei and incident protons.

| Reaction | Energy (MeV) |
|---|---|
| $^{12}C(p,p')^{12}C^*$ | 4.44 |
| $^{12}C(p,2p')\,^{11}B^*$ | 4.44 |
| $^{16}O(p,p'\alpha)\,^{12}C^*$ | 4.44 |
| $^{16}O(p,p')\,^{16}O^*$ | 2.74, 6.13, 7.12 |
| $^{16}O(p,pp)^{15}N^*$ | 5.27 |

emission rate was kept low so that the fraction of random events was negligible. In order to achieve a more accurate tracking of the gammas and electrons in the detection volumes, the Livermore polarized low energy electromagnetic physics was used instead of the standard physics list. The low energy physics takes into account Doppler broadening that may have an effect on the reconstructed spatial resolution. In order to reflect experimental data, when a particle interacts within one crystal, either through single or multiple interactions, the position is assigned to the centroid of the energies deposited. Thus multiple interactions are not reconstructed independently. Other simulated effects such as pair-production, energy loss mechanisms (e.g. high energy knock-on electrons escaping the sensitive volume), Bremsstrahlung photons, and multiple interactions within the same scintillating crystal can deteriorate the reconstructed spatial resolution and are strongly dependent on the incident gamma ray energy and on the secondary production thresholds applied in simulations. In this study a threshold of ~10 keV for photons and ~160 keV for electrons and positrons was applied. A study of the different interaction types at different incident gamma energies is presented in section 3.2. The impact on spatial resolution of these effects can be quantified through Monte Carlo simulations, and is currently under study. Additionally these simulations were employed to test the spectral image reconstruction algorithm described in section 2.5 which was used to reconstruct experimental data.

*2.4.3. 150 MeV protons on PMMA target.* A mono-energetic 150 MeV proton beam was simulated impinging on a PMMA target, as described in section 2.3. The proton intensity was set to $9 \cdot 10^7$ protons $s^{-1}$, close to the experimental value. The purpose of these simulations was to inspect the detected radiation, in terms of energy and particle type, in order to optimize the background rejection in measured samples. As described in Ortega *et al* (2015) comparable amounts of neutrons and prompt gammas escape the phantom after proton irradiation. Both particles yield double and triple-interaction events in the Compton telescope. The fraction of two- and three-interaction events by incident prompt gammas is in average 4.5 times larger than those yielded by neutrons and this ratio varies with the proton beam energy. It is necessary to set energy selection criteria to minimize the background in the images.

## 2.5. Spectral image reconstruction

During image reconstruction, measured data were used to determine the most likely configuration of prompt gamma emissions over the field of view—or image space. In image reconstruction from Compton camera data the list-mode ML-EM algorithm is most appropriate. The algorithm is given by:

$$n_j^{k+1} = \frac{n_j^k}{s_j} \sum_{i \in M} \frac{a_{ij}}{\sum_{j=1}^{J} a_{ij} n_j^k}, \tag{2}$$

where $n_j^k$ is the estimated emission distribution in image element $j \in \{1, ...., J\}$ at iteration $k$ and $a_{ij}$ is the system matrix for measurement $i$ at image element $j$. The sensitivity to measurement for each voxel is given by $s_j$ and the summation is over all measured cone-surfaces $M$. These cone-surfaces can be deduced for each measurement provided the first two interaction points and the initial energy, $E_0$, are known. However, when only two interactions are measured, $E_0$ is unknown. This ignorance is relevant since the prompt gammas are emitted over a wide spectrum of energies. $E_0$ may be computed for events comprising three or more sequential interactions of a single photon. However, the main component of the data is made up of events with only two measured interactions, which do not convey enough information to deduce $E_0$. Consequently, an algorithm must be used that properly takes into account that for each prompt gamma we ignore its emission point, $\vec{x}$, as well as its emission energy, $E_0$. Naturally, this can be achieved by extending the standard three dimensional, spatial, distribution to four dimensions; three spatial and one spectral, $(\overline{x}, E)$ (Xu and He 2007). The final image space was composed of spatial-spectral voxels, with each element $j$ constituting a small image-volume element at specific energy making up a four dimensional pixel located at $(\overline{x}, E)$. The value of the system matrix, $a_{ij}$, at each image space element $j$ was determined using a Gaussian distribution, described over the distance between each pixel location, $\overline{x}$, and the cone surface determined by the pixel energy $E$. Effectively, for each list-mode measurement $i$, a three dimensional estimate of possible emission locations was determined for each possible emission energy $E_0$, creating a four dimensional estimate of the possible emission location-energies: $a_{ij}$. The cone-surface corresponding to any given $E_0$ was Gaussian with uniform width over all energies. The spatial-spectral system matrix elements $a_{ij}$ corresponding to each measurement $i$ can be used directly in equation (2) without change to the algorithm. More details regarding the implementation of this spatial-spectral image space to Compton camera image reconstruction for prompt gamma imaging in hadron therapy monitoring can be found in Gillam *et al* (2011).

As the spectral dimension extends over two orders of magnitude the voxel sizes were allocated with log-based scaling in the spectral domain to reduce the computational burden. Such
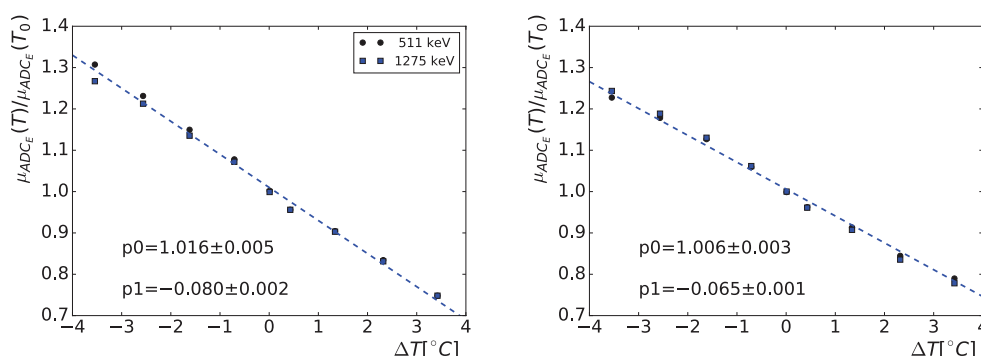
**Figure 4.** Position of the 511 keV (black circles) and 1275 keV (blue squares) photo-peaks as a function of the temperature variation. The reference temperature $T_0$ is 24.5 °C. The two graphs refer to the first layer (left) and the second layer (right). The dashed line represents the linear fit whose parameters are also indicated.

non-uniform sampling of $E_0$ within the image space was also advantageous because at higher emission energies, the change in cone surface half-angle, as a function of $E_0$, is reduced so that voxels with larger spectral spacing are more appropriate. In this investigation the spectral dimension of the image space ranged from 1 MeV to 14 MeV divided into 100 logarithmically spaced bins. The three spatial dimensions of the image space were divided into equally spaced Cartesian voxels. In order to enhance the computational speed, the code was implemented using GPU hardware, with software based on PyCUDA (Klöckner *et al* 2012). Because the location of the hadron beam was of primary interest, after reconstruction the four dimensional images were summed over the spectral dimension to allow analysis within a three dimensional volume. While such summation was generally conducted over the full spectral domain, in some cases the summation only included a subset of relevant spectral slices.

## 3. Results and discussion

### 3.1. Detector energy and temperature calibration

The temperature calibration of the detectors was carried out as described in section 2.2. Figure 4 shows the photo-peak position at 511 keV and 1275 keV acquired at different temperatures. The value of the temperature coefficient $\alpha$ was $-8.0\%$ °C$^{-1}$ and $-6.5\%$ °C$^{-1}$ for the first and second layer, respectively. Figure 5 shows the measured spectra of a $^{22}$Na point-like source acquired in single mode by the two-layer system. The spectra were measured at 24.5 °C and the energy resolution at 511 keV is 8.1% and 8.3% in the first and second layer, respectively.

In order to calibrate the detector at higher energies, the spectra measured in single mode with the Am-Be source were compared to the simulated source, as shown in figure 6. From comparison, the high energy peak in the experimental data can be associated with the 4.44 MeV double-escape peak. The disagreement most likely arises from background signals as well as neutron source emission, since the emission spectrum can be affected by the source container and surrounding materials were not modeled in simulation. Figure 6 (right) shows the energy calibration computed from the $^{22}$Na and Am-Be sources for the second layer and applied in data analysis. The deviation from linearity at 3.44 MeV amounts to 9%. An energy calibration similar to that obtained from the second layer was applied to the first.
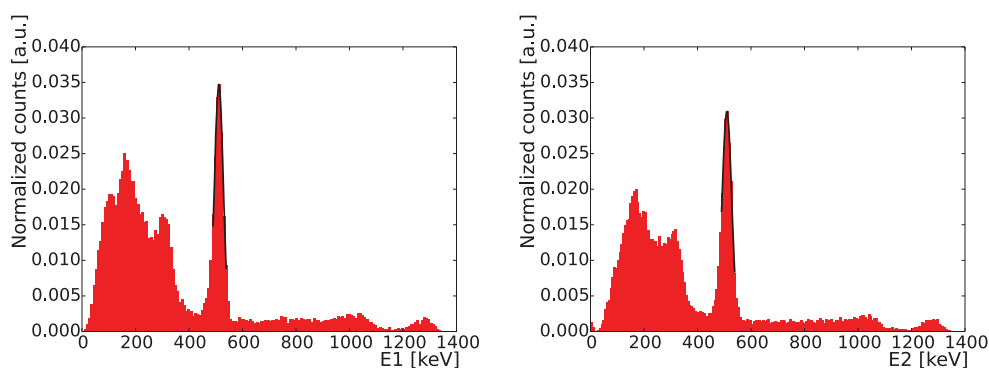
**Figure 5.** Measured calibrated spectra of $^{22}$Na point-like source for the first (left) and second (right) layer of the Compton telescope. The spectra are acquired in a climate chamber at a stable temperature of 24.5 °C.
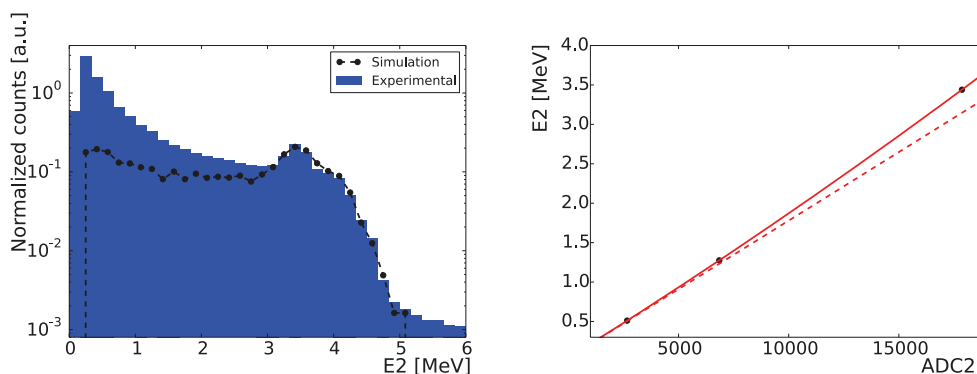


**Figure 6.** Left: the calibrated energy spectrum measured by the second layer irradiated by an Am-Be source is compared to that simulated. The spectra are normalized to the [3, 4] MeV region. The energy calibration applied to experimental data is shown on the right. The solid line represents the actual calibration curve. For comparison the linear fit (dashed line) is also shown.

### 3.2. System efficiency and spatial resolution

From simulations, as described in section 2.4.2, the efficiency and spatial resolution for different mono-energetic gamma ray sources were computed. Gamma rays were isotropically emitted from a point-like source placed 107.5 mm from the surface of the first detector layer. The fraction of coincidences between the three layers (1–2–3) is of only a few percent (figure 7, top left). Two-interaction events between the second and third layers (2–3) represent about 50% of coincidence events because of the smaller distance between the two detectors and the larger thickness of the last device. The percentage of two-interaction events in the first two layers ranges between 30% and 40%. The efficiency of an emitted gamma ray at a given energy to yield a double interaction in the first and second detector layers ranges from $6.9 \cdot 10^{-6}$ to $2.5 \cdot 10^{-5}$, (from low to high energy) without any energy selection on detected events (see figure 7, right). Two energy thresholds were considered to study their impact on the efficiency and spatial resolution of the reconstructed sources. If an energy threshold of 1 MeV was applied to the sum of the two interactions an efficiency loss of 20% at 2.74 MeV and 3% at 7.12 MeV was observed. The efficiency drops drastically if a 0.5 MeV threshold was
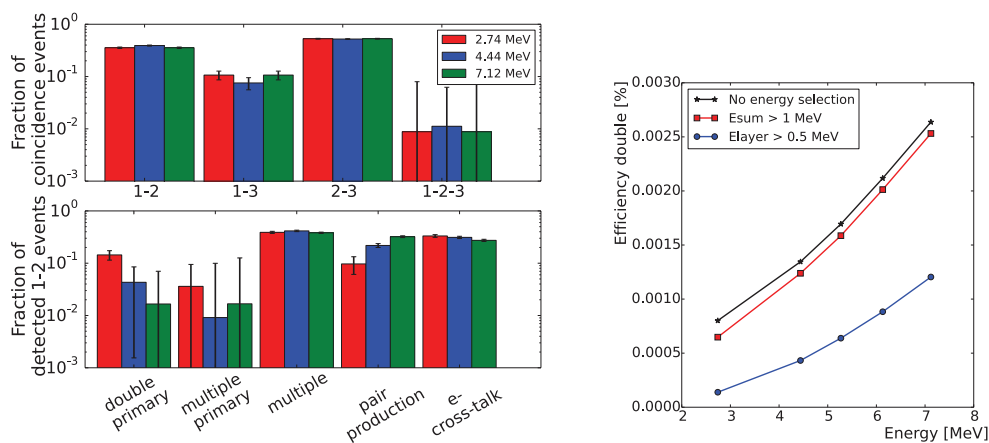
**Figure 7.** Top left: detector layer multiplicity of the detected coincidence events. Bottom left: interaction experienced by detected photons yielding a coincidence between the first and second layers. Right: percentage of detected gamma rays at different incident energies (see table 2) yielding a coincidence between the first two layers of the Compton telescope after applying different energy thresholds.

applied to each detector with a loss of 50% of coincidences at the highest energies. Efficiency was computed from the fraction of events undergoing a double interaction in the two layers over the total number of emitted photons, without applying any further condition. That means that pair-production and Compton scattering both contribute to total efficiency. According to NIST data[8], at 2 MeV the Compton scattering probability in $LaBr_3$ is one order of magnitude larger than pair production. The two cross sections are comparable at 7 MeV.

The fraction of Compton scattered photons yielding two interactions in the two layers would also be affected by the probability that the scattered gamma ray exits one detector and interacts again in the second device. This contribution increases with the incoming gamma energy. The study of the type of interactions experienced by a gamma that yields a signal in the first and in the second detector layers is summarized in figure 7 (bottom left). Double events (*double primary*) correspond to either a Compton interaction per detector or a Compton and photo-electric event experienced by the incident photon. These are considered as *golden* events and are statistically significant only at the lower energy. The probability that an incident photon undergoes multiple interactions within one or both detector layers (*multiple primary*) is a few percent. Multiple Compton and photo-electric interactions experienced by primary and secondary photons (*multiple*) is ∼40%. Secondary photons are produced via bremsstrahlung by Compton scattered e- whose energy increases with the incident gamma energy. At the higher energies interactions are dominated by the probability that the photon undergoes pair-production. At the highest energy up to 30% of the detected events are due to pair-production. It is also important to notice that more than 90% of the Compton–Compton *golden* events were forward oriented. However when dealing with Compton-photoelectric events the forward fraction drops below 50%. The lowest energy of the back-scattered photon increases the probability of photo-electric absorption. About 30% of double-interactions are associated with signal deposited by an electron produced in one layer then being detected in the second. The fraction of these events is sensitive to the secondary production thresholds applied in the simulation and to the energy threshold applied to each detector layer in the coincidence selection.
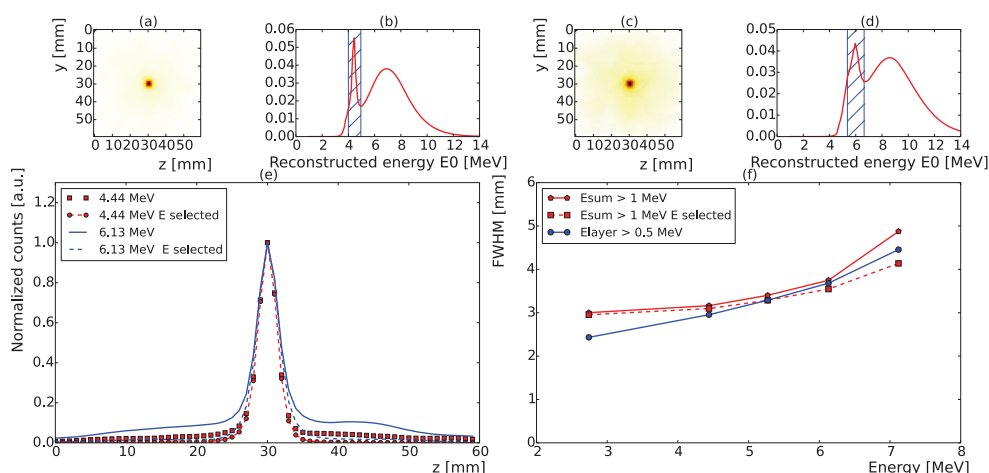
[8] http://physics.nist.gov.

**Figure 8.** (a)–(c) Reconstructed images of the point-like sources emitting 4.44 MeV and 6.13 MeV gamma rays, respectively integrated over the spectral dimension (iteration 20). (b)–(d) Distribution of the reconstructed gamma ray energy as obtained from the spectral reconstruction of the monochromatic sources (4.44 MeV and 6.13 MeV, respectively) after 3D spatial integration of the image. The blue dashed area indicates the energies selected in the spectral domain to study the impact of the reconstructed energy on the spatial resolution, as shown in (e). (e) Profiles of the reconstructed point-like sources at 4.44 MeV and 6.13 MeV energy. The source profiles are obtained after integrating the image over a central region with $\Delta y = 2$ mm. The solid line refers to the integration over the full spectral range, while the dashed line stands for integration in the spectral dimension over a window centered at the gamma ray emission energy (blue dashed area in (b) and (d)). (f) Spatial resolution (FWHM) estimated from the reconstructed profiles at different incident energies of the gamma rays and for different energy thresholds.

The point-like sources were reconstructed using the spectral reconstruction algorithm. In figures 8(a) and (c) the reconstructed images at two incident gamma energies, 4.44 MeV and 6.13 MeV, are shown. The image space was $3 \times 160 \times 160$ mm$^3$ with voxel size of $3 \times 1 \times 1$ mm$^3$. As shown in figure 8(e), the reconstruction of incorrect energies of the incoming gamma rays introduces a smooth background. Spatial resolution ranges from 3.0 mm (FWHM) at the lowest energies to 4.9 mm (FWHM) at 7.12 MeV (figure 8(f)). The application of energy selection criteria over the spectral dimension after image reconstruction improves the spatial resolution by 0.8 mm at high energies. The application of a 0.5 MeV energy threshold at the detector level improves by 0.6 mm the spatial resolution at the lowest energy yet significantly reduces the detection efficiency (see figure 7). The degradation of the spatial resolution with increasing energy is affected by the larger fraction of gamma rays undergoing pair-production as well as multiple interactions within the same layer. Techniques to identify patterns in the detected events to reject pair production are under investigation and are expected to improve the reconstructed spatial resolution. Pair-production events can be also reconstructed, as described in Rohling *et al* (2015) where the potential of a combined pair-production—Compton camera is described.

### 3.3. Proton irradiation of PMMA target

As described in section 2.3, a PMMA target was irradiated by 150 MeV protons at a current of $9 \cdot 10^7$ protons s$^{-1}$. The spectra were measured first in single mode and the energy calibration shown in figure 6 was applied. Given the non-negligible deviation from linearity at
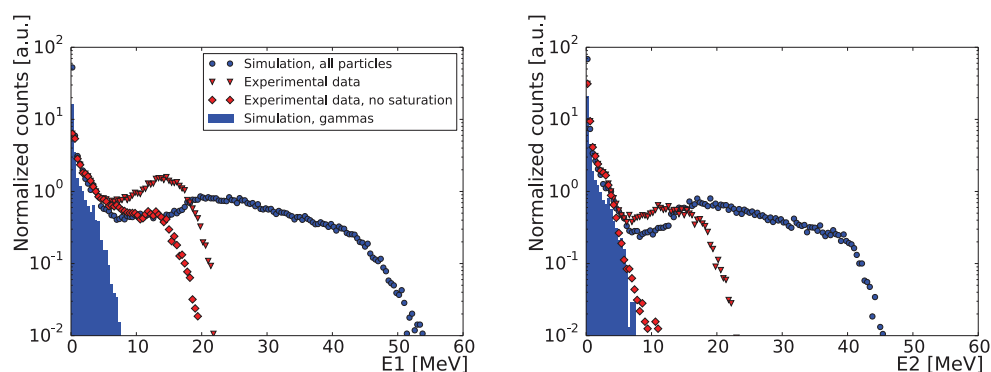
**Figure 9.** Simulated and measured energy spectra acquired in single mode for the first (left) and second (right) layers after 150 MeV proton interaction in a PMMA target. The simulated spectrum of all detected secondary particles is compared to the energy distribution of gamma rays produced by proton inelastic interactions. The measured spectrum is provided before and after the rejection of data with saturated pixels (no saturation), causing an efficiency loss at the highest energies.

energies above 2 MeV, measured data were also selected in order to avoid saturation effects. The dynamic range of each MPPC was determined directly from experimental data and all events yielding one or more saturated pixels were removed from the data. Figure 9 shows the comparison between measurements and simulations. Simulated data have been processed in order to show the contribution of gamma rays. While the energy deposited by gamma rays does not exceed 10 MeV in either detector, hadrons (mostly neutrons) deposit energy up to about 50 MeV and show a peak at 20 MeV. According to Monte Carlo simulations the rate of particles exiting the PMMA phantom and reaching the first layer is $5 \cdot 10^{-4}$ n/proton and $4 \cdot 10^{-4}$ $\gamma$/proton. The two rates are comparable on the second layer, amounting to about $2 \cdot 10^{-4}$ particle per incident proton. The mean neutron energy is 20 MeV, one order of magnitude larger than the mean prompt gamma energy. The highest-energy neutrons are mostly forward oriented (Robert *et al* 2013). However the reader should be aware that discrepancies have been reported between the used physics list and the prompt gamma production yields experimentally measured. In Schumann *et al* (2015) the QGSP_BIC_HP Geant4 hadronic list is validated against experimental data from proton irradiation. The prompt gamma yield is significantly overestimated, while the overall shape of the emission prompt gamma spectrum is accurately reproduced. The detector signal is fully saturated at about 20 MeV, but even at 3 MeV pixel saturation causes the rejection of few events that might be otherwise incorrectly reconstructed in terms of energy and position.

The PMMA phantom was also measured in coincidence mode at two different locations, $\pm 5$ mm, in order to study the capability to detect shifts of the Bragg peak. The set-up was also simulated in order to study background rejection criteria in coincidence mode. Simulated coincidences were sorted and identified as either true or random. Figure 10 shows the fraction of true coincidences over the total number of detected coincidences as a function of the sum of the energy deposited in the two detector layers. In order to reconstruct the prompt gamma emission profile saturated events were rejected. A 0.5 MeV threshold was applied at detector level. Events were further filtered by applying an energy window of 1–7 MeV to the sum of the deposited energies in the two detectors. This energy selection retains the optimal 2–6 MeV energy window where, according to figure 10, the true coincidence ratio achieves the highest value, while preserving statistics in the reconstructed data (about 18 000 and 28
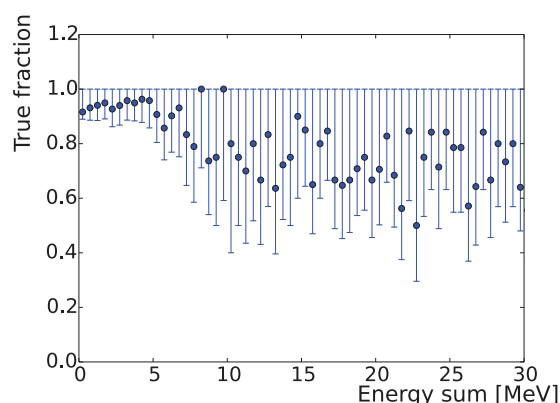
**Figure 10.** Ratio of the true double coincidences over the total number of double coincidences sorted with a 40 ns coincidence window from simulations of 150 MeV protons interacting in a PMMA phantom. The uncertainties are computed from the Poisson statistics of the simulated samples.
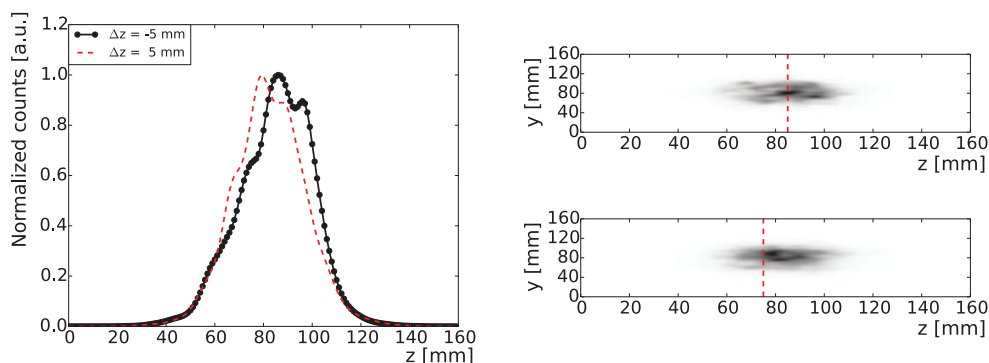


**Figure 11.** Left: reconstructed profiles at iteration 10 of the prompt gamma emission vertices within the PMMA phantom irradiated by 150 MeV proton beam. Right: 2d reconstructed images of the prompt gamma emission vertices. The red dashed line indicates the expected position of the Bragg Peak. The images have been reconstructed with a field of view of $3 \times 160 \times 160$ mm$^3$ with $3 \times 1 \times 1$ mm$^3$ voxel. The source profiles are obtained after integrating the image over a central region with $\Delta y = 20$ mm. As described in figure 2, the beam direction is $-\vec{z}$.

000 coincidences were reconstructed in the $-5$ mm and $+5$ mm configuration, respectively). The reconstructed Bragg peak profiles are shown in figure 11. The reconstructed images were summed over the spectral domain between 4.1 MeV and 4.6 MeV, in order to select the 4.44 MeV prompt gamma emission energy. The shift of the Bragg peak location is visible in the reconstructed profiles and amounts to 7 mm (computed from the maximum of the profiles). This result indicates the capability of the two-layer version of the MACACO Compton telescope to assess range variations.

## 4. Conclusions

Real-time range assessment in ion-beam therapy becomes more important in hypofractionated treatments where the need of a fast feedback on the treatment delivery is crucial.

Electronically collimated gamma cameras can indirectly verify, in real-time, the ion range in patient tissues through the detection of prompt gammas emitted within few ps after the passage of the primary ion. In this investigation the characteristics of the MACACO Compton telescope have been described based on both measurements and Monte Carlo simulations of the detector. The potential of the Compton telescope to detect range variations in proton irradiation of a tissue equivalent target has been demonstrated. However quantitative range assessment entails further enhancements to the electronics and event selection algorithms. The detector performance was limited by poor time resolution (25 ns FWHM in coincidence mode) that required the use of a wide coincidence window. Efforts are now being invested towards the improvement of the timing performance of the detector in order to reduce the width of the coincidence window.

Despite the abundance of emitted prompt gammas, sensitivity still remains an issue in Compton camera measurements. The first limitation to count statistics arises from the limited acceptance angle of Compton cameras, that could be partially mitigated through replicated devices encircling the patient. Attempts to optimize the electronics and detector design should be accompanied by enhancements to developing software. Dedicated image reconstruction approaches have been developed to deal with double coincidence events with unknown incident energy of the gamma ray. As discussed, the integration of the spectral dimension into the image space significantly increases the computational cost which requires further speed enhancements to cope with real-time range verification. A major challenge is represented by the variety and complexity of interaction modes of the incident gamma within the detection system together with the background arising mostly from neutrons. As discussed in sections 3.2 and 3.3, optimized energy thresholds can mitigate this problem. Background rejection can be improved by the use of an hodoscope tracking the direction of the incoming ion beam. The information extracted from the hodoscope can improve the localization of the reconstructed prompt gamma vertices and trigger the acquisition of the Compton telescope. Finally, in order to fully exploit the potential of a three-layer Compton telescope, software integration to merge the reconstruction of two and three interaction events requires investigation in order to benefit from both the larger statistical abundance of double coincidences and the more accurate knowledge obtained using the prompt gamma emission energy from triple coincidences.

## Acknowledgments

## References

Agostinelli S *et al* 2003 Geant4—a simulation toolkit *Nucl. Instrum. Methods* A **506** 250–303
Barrio J, Etxebeste A, Lacasta C, Muñoz E, Oliver J, Solaz C and Llosá G 2015 Performance of VATA64HDR16 ASIC for medical physics applications based on continuous crystals and SiPMs *J. Instrum.* **10** P12001
Cabello J, Etxebeste A, Llosá G and Ziegler S I 2015 Simulation study of PET detector limitations using continuous crystals *Phys. Med. Biol.* **60** 3673–94

Enghardt W *et al* 1999 Positron emission tomography for quality assurance of cancer therapy with light ion beams *Nucl. Phys.* A **654** 1047c

Gillam J E, Lacasta C, Torres-Espallardo I, Candela Juan C, Llosá G, Solevi P, Barrio J and Rafecas M 2011 A Compton imaging algorithm for on-line monitoring in hadron therapy *Med. Imaging* **7961** 79611O

Golnik C *et al* 2014 Range assessment in particle therapy based on prompt γ-ray timing measurements *Phys. Med. Biol.* **59** 5399–422

Jan S *et al* 2004 Gate: a simulation toolkit for PET and SPECT *Phys. Med. Biol.* **49** 4543–61

Klöckner A, Pinto N, Lee Y, Catanzaro B, Ivanov P and Fasih A 2012 PyCUDA and PyOpenCL: a scripting-based approach to GPU run-time code generation *Parallel Comput.* **38** 157–74

Knopf A and Lomax A 2013 *In vivo* proton range verification: a review *Phys. Med. Biol.* **58** R131–60

Kormoll T, Fiedler F, Schóne S, Wüstemann J, Zuber K and Enghardt W 2011 A Compton imager for *in vivo* dosimetry of proton beams–a design study *Nucl. Instrum. Methods* A **626–7** 114–9

Li Z, Wedrowski M, Bruyndonckx P and Vandersteen G 2010 Nonlinear least-squares modeling of 3D interaction position in a monolithic scintillator block *Phys. Med. Biol.* **55** 6515–32

Llosá G, Trovato M, Barrio J, Etxebeste A, Munoz E, Lacasta C, Oliver J F, Rafecas M, Solaz C and Solevi P 2016 First images of a three-layer compton telescope prototype for treatment monitoring in hadron therapy *Front. Oncol.* **6** 14

Llosá G *et al* 2013a First Compton telescope prototype based on continuous LaBr3-SiPM detectors *Nucl. Instrum. Methods* A **718** 130–3

Llosá G *et al* 2013b Second LaBr3 Compton telescope prototype *Conf. Record of the 3rd Int. Conf. ANIMMA* pp 1–4

Marsh J W, Thomas D J and Burke M 1995 High resolution measurements of neutron energy spectra from Am-Be and Am-B neutron sources *Nucl. Instrum. Methods* A **366** 340–8

Meier D *et al* 2010 An ASIC for SiPM/MPPC readout *IEEE Nuclear Science Symp. Medical Imaging Conf.* pp 1653–7

Min C H, Kim C H, Youn M Y and Kim J W 2006 Prompt gamma measurements for locating the dose falloff region in the proton therapy *App. Phys. Lett.* **89** 183517

Ortega P G *et al* 2015 Noise evaluation of Compton camera imaging for proton therapy *Phys. Med. Biol.* **60** 1845–63

Peterson S W, Robertson D and Polf J 2010 Optimizing a three-stage Compton camera for measuring prompt gamma rays emitted during proton radiotherapy *Phys. Med. Biol.* **55** 6841–56

Pinto M *et al* 2015 Absolute prompt-gamma yield measurements for ion beam therapy monitoring *Phys. Med. Biol.* **60** 565–94

Pinto M, Dauvergne D, Freud N, Krimmer J, Letang J M, Ray C, Roellinghoff F and Testa E 2014 Design optimisation of a TOF-based collimated camera prototype for online hadrontherapy monitoring *Phys. Med. Biol.* **59** 7653–74

Polf J C, Avery S, Mackin D S and Beddar S 2015 Imaging of prompt gamma rays emitted during delivery of clinical proton beams with a Compton camera: feasibility studies for range verification *Phys. Med. Biol.* **60** 7085–99

Polf J C *et al* 2009 Measurement and calculation of characteristic prompt gamma ray spectra emitted during proton irradiation *Phys. Med. Biol.* **54** N519–27

Robert C *et al* 2013 Distributions of secondary particles in proton and carbon-ion therapy: a comparison between GATE/Geant4 and FLUKA Monte Carlo codes *Phys. Med. Biol.* **58** 2879–99

Rohling H, Golnik C, Enghardt W, Hueso-González F, Kormoll T, Pausch G, Schumann A and Fiedler F 2015 Simulation study of a combined pair production—compton camera for *in vivo* dosimetry during therapeutic proton irradiation *IEEE Trans. Nuclear Science* **62** 2023–30

Schardt D, Elsässer T and Schulz-Ertner D 2010 Heavy-ion tumor therapy: physical and radiobiological benefits *Rev. Mod. Phys.* **82** 383–425

Schumann A, Petzoldt J, Dendooven P, Enghardt W, Golnik C, Hueso-González F, Kormoll T, Pausch G, Roemer K and Fiedler F 2015 Simulation and experimental verification of prompt gamma-ray emissions during proton irradiation *Phys. Med. Biol.* **60** 4197–207

Shakirin G, Braess H, Fiedler F, Kunath D, Laube K, Parodi K, Priegnitz M and Enghardt W 2011 Implementation and workflow for PET monitoring of therapeutic ion irradiation: a comparison of in-beam, in-room, and off-line techniques *Phys. Med. Biol.* **76** 1281–98

Smeets J *et al* 2012 Prompt gamma imaging with a slit camera for real-time range control in proton therapy *Phys. Med. Biol.* **57** 3371–405

Stankova V, Barrio J, Gillam J E, Lacasta C, Rafecas M, Solaz C, Trovato M and Llosá G 2012 Multichannel DAQ system for SiPM matrices *IEEE Nuclear Science Symp. Medical Imaging Conf.* pp 1069–71

Verburg J M, Riley K, Bortfeld T and Seco J 2013 Energy- and time-resolved detection of prompt gamma-rays for proton range verification *Phys. Med. Biol.* **58** L37–49

Xu D and He Z 2007 Gamma-ray energy-imaging integrated spectral deconvolution *Nucl. Instrum. Methods* A **574** 98–109